

Graphene Modified Tin Dioxide for Efficient Planar Perovskite Solar Cells with Enhanced Electron Extraction and Reduced Hysteresis

Menghua Zhu, Weiwei Liu, Weijun Ke, Lisha Xie, Pei Dong, and Feng Hao

ACS Appl. Mater. Interfaces, **Just Accepted Manuscript** • DOI: 10.1021/acsami.8b15665 • Publication Date (Web): 10 Dec 2018

Downloaded from <http://pubs.acs.org> on December 10, 2018

Just Accepted

“Just Accepted” manuscripts have been peer-reviewed and accepted for publication. They are posted online prior to technical editing, formatting for publication and author proofing. The American Chemical Society provides “Just Accepted” as a service to the research community to expedite the dissemination of scientific material as soon as possible after acceptance. “Just Accepted” manuscripts appear in full in PDF format accompanied by an HTML abstract. “Just Accepted” manuscripts have been fully peer reviewed, but should not be considered the official version of record. They are citable by the Digital Object Identifier (DOI®). “Just Accepted” is an optional service offered to authors. Therefore, the “Just Accepted” Web site may not include all articles that will be published in the journal. After a manuscript is technically edited and formatted, it will be removed from the “Just Accepted” Web site and published as an ASAP article. Note that technical editing may introduce minor changes to the manuscript text and/or graphics which could affect content, and all legal disclaimers and ethical guidelines that apply to the journal pertain. ACS cannot be held responsible for errors or consequences arising from the use of information contained in these “Just Accepted” manuscripts.

Graphene Modified Tin Dioxide for Efficient Planar Perovskite Solar Cells with Enhanced Electron Extraction and Reduced Hysteresis

Menghua Zhu,^a Weiwei Liu,^a Weijun Ke,^b Lisha Xie,^a Pei Dong,^c Feng Hao^{*a}

^a School of Materials and Energy, University of Electronic Science and Technology of China, Chengdu 610054, China. E-mail: haofeng@uestc.edu.cn

^b Department of Chemistry, Northwestern University, 2145 Sheridan Road, Evanston, Illinois 60208, United States

^c Department of Mechanical Engineering, George Mason University, Virginia, VA 22030, USA

Abstract

Tin dioxide (SnO₂) as an efficient electron transport layer (ETL) has been demonstrated for emerging high performance organic-inorganic hybrid perovskite solar cells (PSCs). However the low temperature solution-processed SnO₂ usually results in high trap-state density and current-voltage hysteresis. Here we reported an effective strategy to solve this problem by incorporation graphene ink to the low temperature processed SnO₂ for planar structure PSCs. The electron extraction efficiency has been significantly improved with graphene doped SnO₂ ETL coupled with attenuated charge recombination at the ETL/perovskite interface. The power conversion efficiency of PSCs based on graphene-SnO₂ ETL reached over 18% with negligible hysteresis. Incorporation of graphene into the ETL layer also enhanced the device stability retaining 90% of the initial PCE value after storing in ambient condition with a relative humidity of 40 ± 5% for 300 hours. Our results provide important insight for further efficiency boost in SnO₂ based low-temperature processed PSCs.

Keywords: graphene ink, low temperature process, trap state, charge recombination, stability

1. Introduction

Hybrid halide perovskites solar cells (PSCs) are promising candidates for solving the impending energy shortage, and therefore have attracted great attention as next-generation solar cells with low cost and high performance.¹⁻³ The power conversion efficiency (PCE) of PSCs has rapidly exceeded 23% via controlled crystal film growth, interface and device engineering.⁴⁻⁶ The perovskite materials with hybrid organic-inorganic nature guarantees the superior carrier mobility and the processability.⁷ So far, the mainstream development of PSC is based on methylammonium lead iodide ($\text{CH}_3\text{NH}_3\text{PbI}_3$), featuring sufficient carrier diffusion lengths and high absorption coefficients,^{8, 9} as well as high charge carrier mobilities.¹⁰ Essential components in the device structure of a PSC include a n-type and p-type charge-selective contact. TiO_2 is used as the majority n-type contact in regular structured devices, either acting as a thin compact layer in a planar configuration,¹¹ or in a mesostructured configuration.¹² However, due to the notorious hysteresis effects,¹³⁻¹⁵ interface engineering of TiO_2 with ionic liquids^{16, 17} or fullerenes^{18, 19} has been proposed accordingly. On the other hand, SnO_2 has recently been recognized as an efficient n-type contact alternative with excellent steady state performances.²⁰⁻²² Compared with the benchmark TiO_2 , SnO_2 shows several advantages such as wider bandgap (ranging from 3.6 to 4.1 eV), higher carrier mobility ($240 \text{ cm}^2/(\text{V}\cdot\text{s})$), chemical stability and lower conduction band, which make it promising for planar PSCs with higher performance.²³ The lower conduction band and better mobility ensure more efficient carrier transport.^{24, 25} Many efforts have been made to prepare low temperature SnO_2 films including spin-coating solution,²⁵ dual-fuel combustion,²⁶ chemical-bath deposition (CBD),²⁷ and atomic layer deposition (ALD).²⁸ Compared to the high temperature annealed TiO_2 ETL (usually $\geq 500 \text{ }^\circ\text{C}$), SnO_2 ETL from low-temperature process makes it more appealing for flexible application by

1
2
3 roll-to-roll printing. Unfortunately, majority of these devices suffer from serious hysteresis.
4
5 The existing primary mechanisms of the J - V hysteresis character of PSCs include: trapping
6
7 and detrapping of charge carriers, slow transient capacitive current and band bending owing
8
9 to ferroelectric polarization or ion migration.²⁹⁻³⁴ It has been demonstrated that the
10
11 hysteresis behavior can be effectively suppressed by improving charge carrier collection
12
13 efficiency at interfaces of ETL/perovskite or HTL/perovskite³⁵⁻³⁹. However, most of these
14
15 methods are either relatively expensive or using hazardous materials.
16
17

18
19
20 In this study, we reported a low-temperature processed graphene ink doped SnO₂ for planar
21
22 PSCs. The electron extraction efficiency has been significantly improved with the graphene
23
24 ink doped SnO₂ ETL coupled with attenuated charge recombination at the ETL/perovskite
25
26 interface. It is found that the graphene-SnO₂ device exhibited superior efficiency over 18%.
27
28 The J - V hysteresis in the device is remarkably attenuated mainly correlated with the
29
30 enhanced electron mobility and electron extraction through the incorporation of the
31
32 two-dimensional electronic conducting graphene in the SnO₂ matrix. More significantly, the
33
34 graphene-SnO₂ ETL provides a remarkable improvement in stability, retaining ~90%
35
36 performance after aging in air for 300 hours due to the hydrophobicity nature of graphene.
37
38
39
40
41
42
43
44

45 **2. Results and Discussion**

46
47 Graphene ink was synthesized by liquid phase exfoliation,⁴⁰ the details can be found in the
48
49 Experimental section. The graphene layer was confirmed by AFM image and Raman spectra
50
51 (Figure S1 and S2). SnO₂ layers were spin cast on FTO glass substrates (shown in Figure 1a).
52
53 Top views of scanning electron micrographs (SEM) with different ETLs are shown in Figure
54
55 1b-d. SnO₂ layers (Figure 1b) exhibit similar features compared to the FTO substrate (Figure
56
57 S3) because of the conformal nature of the deposition process. The SnO₂-graphene layer by
58
59
60

1
2
3 solution processed spin coating is presented in Figure 1c. An obvious clear change in the
4 morphology of the substrate is displayed, indicating a rougher surface than the SnO₂ layer,
5
6 evidencing the incorporation of graphene into the SnO₂ layer. Varied amounts of the
7
8 graphene-SnO₂ films were prepared by mixing the graphene stock solutions with the
9
10 SnCl₂·2H₂O/ethanol solutions. With volume ratios of 1, 2 and 4% of the graphene stock
11
12 solutions prepared in the composite precursor solutions, the mass concentrations of
13
14 graphene in SnO₂ of total volume were calculated to be 0.05, 0.1 and 0.2 mg mL⁻¹,
15
16 respectively. Figure S4 shows the SEM images of the graphene-SnO₂ ETLs with volume of
17
18 graphene ranging from 0% to 4%. The perovskite layers are further deposited on the
19
20 graphene-SnO₂ layer composing of large crystals with a grain size of 200-500 nm (Figure 1d),
21
22 forming a dense, smooth, uniform, and pin-hole-free film with well-packed and
23
24 well-crystallized grains. Using this high-quality perovskite film, planar devices were
25
26 fabricated with the configuration of FTO/graphene-SnO₂/MAPbI₃/spiro-OMeTAD/Au.
27
28 Cross-sectional SEM image in Figure 1e showed the thickness is about 50 nm, 400 nm, 200
29
30 nm, 80 nm for the ETL, perovskite layer, spiro-OMeTAD layer, and Au electrode, respectively.
31
32 To determine chemical state of the as-prepared SnO₂, we used the X-ray photoelectron
33
34 spectroscopy (XPS) to probe the chemical states of SnO₂-graphene film. XPS spectra (Figure
35
36 2) exhibit the survey of elements and the high resolution of Sn, O and Cl confirms the
37
38 formation of pure SnO₂ observing the oxygen peak O 1s at 531.0 eV, Sn⁴⁺ (Sn 3d_{5/2} and Sn
39
40 3d_{3/2}) peaks at 495.3 eV as well as at 486.8 eV and Cl 2p at 197.6 eV, respectively. As shown
41
42 in Figure 2d, only trace amounts of Cl in the SnO₂ film indicates nearly complete conversion
43
44 of the SnCl₂ precursor to SnO₂.
45
46
47
48
49
50
51
52
53
54
55
56

57 Figure 3a shows the optical transmission spectra of the FTO/SnO₂ samples before and after
58
59 graphene incorporation. Both samples display high transmittance of about 80% within the
60

1
2
3 visible range of 400–800 nm. It should be noted that the SnO₂ nanocrystalline film from
4
5 low-temperature process is able to improve the optical transmission properties of the FTO
6
7 substrate.⁴⁰ In our case, the incorporation of a small amount graphene into the SnO₂
8
9 electrode showed no discernable impact on transmittance of the electrode, which ensures
10
11 sufficient photon flux reaching to the perovskite layer for light harvesting. To further
12
13 investigate the electron extraction processes, steady-state photoluminescence (PL) spectra
14
15 of the perovskite films was measured (Figure 3b). The PL spectrum peak at 767 nm agrees
16
17 well with the previous reports.⁴¹ Note that PL spectra on both SnO₂ and graphene-SnO₂
18
19 sample was normalized with their respective absorbance to account for difference in film
20
21 thicknesses. We note that the PL is obviously quenched and sensitive to the incorporation of
22
23 graphene. The PL intensity of perovskite films reduced with the graphene results from
24
25 efficient charge carrier extraction by the graphene flakes in the SnO₂ film.
26
27
28
29
30
31
32

33 To evaluate PSCs performance based on graphene-SnO₂ as ETLs, the *J-V* performance and
34
35 external quantum efficiency (EQE) are measured as shown in Figure 4a and b, respectively,
36
37 Table 1 summarizes the corresponding photovoltaic parameters. With the incorporation of
38
39 graphene in the SnO₂ electrode, the short-circuit current density (J_{sc}), fill factor (FF), open
40
41 circuit voltage (V_{oc}) and PCE have been improved. The effect of the different graphene in the
42
43 SnO₂ electrodes on the photovoltaic performance has been investigated and the results are
44
45 presented in Figure S5. According to the results, device with 1 vol % graphene showed the
46
47 maximum PCEs with an improvement in J_{sc} from 22.46 mA cm⁻² to 23.46 mA cm⁻², and the
48
49 PCE from 17.01% to 18.11% under reverse scanning direction. The V_{oc} and FF of the devices
50
51 with graphene are slightly increased. The enhanced photovoltaic performances of the
52
53 graphene-SnO₂ based devices are mainly attributed to the enhanced electron extraction in
54
55 the ETL layer and the efficient charge separation at the perovskite/ETL interfaces. However,
56
57
58
59
60

1
2
3 further increase of graphene volume to 4% leads to a poor surface of SnO₂ film (as shown in
4
5 Figure S4 d), resulting in the formation of a poor contact and serious degradation of FF of the
6
7 solar cells. Figure 5b shows the EQE spectra with a broad spectral response in the range of
8
9 350–800 nm for both devices with SnO₂ and graphene-SnO₂ ETLs. The integrated current
10
11 densities showed a current density of 21.9 mA cm⁻² and 22.56 mA cm⁻² for the SnO₂ and
12
13 graphene-SnO₂ device respectively, which closely correlate with the photocurrents in the *J-V*
14
15 curves. The EQE of the graphene doped SnO₂ device reaches to be nearly 90%, whereas the
16
17 EQE for the device in absence of graphene is limited to 80%. To further illustrate the role of
18
19 graphene in the SnO₂ ETL electrode in reducing the hysteresis, we calculate the hysteresis
20
21 index of devices using SnO₂ and graphene-SnO₂ as ETLs follow by equation 1:⁴²
22
23
24
25
26
27

$$\text{hysteresis index} = \frac{J_{\text{RS}}(0.8 V_{\text{oc}}) - J_{\text{FS}}(0.8 V_{\text{oc}})}{J_{\text{RS}}(0.8 V_{\text{oc}})} \quad (1)$$

28
29
30
31 where $J_{\text{FS}}(0.8V_{\text{oc}})$ and $J_{\text{RS}}(0.8V_{\text{oc}})$ represent photocurrent density at 80% of V_{oc} for the
32
33 FS(forward scan) and RS(reverse scan), respectively. The calculated hysteresis index values
34
35 are listed in Table 1. Notably, the hysteresis index for the device with graphene is reduced to
36
37 a remarkably low value of only 0.02 compared to 0.08 for that of bare SnO₂ electrode. As
38
39 mentioned above, the *J-V* hysteretic behavior have been studied intensively in the field of
40
41 PSCs. Various mechanism for the hysteretic effects have been proposed, including grain
42
43 boundaries, charge-trapping and detrapping at interfaces, capacitive, ion migration, and
44
45 ferroelectric effects.⁴³⁻⁴⁶ In our work, the attenuated *J-V* hysteresis in the device with
46
47 graphene is believed to be mainly ascribed to the enhanced electron extraction and electron
48
49 mobility through the incorporation of the two-dimensional electronic conducting graphene
50
51 in the SnO₂ matrix. The steady-state power output of the graphene-SnO₂ based device with
52
53 best performance is shown in Figure 4c, delivering a stabilized PCE of 18.0%, which is close
54
55 to the highest efficiency from the reverse scan derived *J-V* sweep. We also check the
56
57
58
59
60

1
2
3 reliability and reproducibility of our ETLs. Figure S6 shows the PCE histogram collected from
4
5 24 independent cells, revealing that more than half of the cells show PCEs higher than
6
7 18.00% and more than 85% of the devices show PCEs above 17.00% under same conditions,
8
9 which is significantly higher than the control devices without graphene in the ETLs.
10
11

12
13 In addition, we compared the device performance of SnO₂ and grapheme-SnO₂ devices with
14
15 an active device area of 0.39 cm². Figure S7 shows the representative *J-V* curves of the PSCs
16
17 using different ETL thin films under simulated AM 1.5G one sun illumination (100 mW m⁻²)
18
19 with the derived performance parameters summarized in the inset. The device with
20
21 graphene-SnO₂ showed a higher PCE (16.17%) than the cells using blank SnO₂ ETL
22
23 (PCE=13.72%), due to a increase in *V*_{oc} and FF. Note that a decent FF of 0.68 for
24
25 graphene-SnO₂ based PSCs indicates more efficient charge carriers extraction is obtained
26
27 within such device.
28
29
30
31
32

33
34 To further assess the lifetime of photoexcited carriers, time-resolved photoluminescence
35
36 spectroscopy (TRPL) was conducted. Figure 4d shows PL decay profiles of the perovskite
37
38 layers on SnO₂ and graphene-SnO₂ ETLs. The electron transfer rates are ultrafast for both
39
40 samples compared to previous reports employing TiO₂ as the ETL.⁴⁷ For further verification,
41
42 the corresponding TRPL spectra of these perovskite films were also measured. Two time
43
44 components were observed for both ETLs by fitting the TRPL curves with biexponential
45
46 decay,⁴⁸
47
48
49

$$f(x) = A_i \sum e^{-t/\tau_i} + B \quad (2)$$

50
51 where *A*_{*i*}, τ_{*i*} and *B* represent for the decay amplitude, decay time and the constant for the
52
53 base-line offset, respectively. The electron transfer rate from the perovskite to
54
55 FTO/graphene-SnO₂ (2.1 ± 0.2 ns) is significantly faster than that for FTO/SnO₂ (4.3 ± 0.2 ns),
56
57
58
59
60

1
2
3 indicating more efficient charge transfer rate due to the incorporation of graphene into the
4
5 SnO₂ matrix. Such correlation of decreased PL efficiency and decreased carrier lifetime with
6
7 graphene doping has been reported earlier in ETLs with incorporated graphene quantum
8
9 dots in compact TiO₂^{49,50}, reduced graphene oxide incorporated in ZnO nanoparticle ETL⁵¹,
10
11 triblock fullerene derivative imbedded in compact TiO₂ ETLs⁵².
12

13
14
15 The interfacial recombination reactions within devices with or without graphene are further
16
17 analyzed by investigating the relationships between the incident light intensity and
18
19 photoelectric response. As shown in Figure 5, the underlying recombination process can be
20
21 analyzed by plotting J_{sc} and V_{oc} as a function of incident light intensity (I) with the following
22
23 equations (3) and (4):^{53, 54}
24
25

$$J_{sc} \propto I^{\alpha} \quad (\alpha \leq 1) \quad (3)$$

$$V_{oc} = \frac{\varepsilon k T \ln(I)}{q} + \text{constant} \quad (4)$$

26
27
28 where T is the absolute temperature, k is the Boltzmann constant, q is the elementary
29
30 charge, and α and ε are the ideal factors relevant to recombination. Under short-circuit
31
32 condition, bimolecular recombination is expected to be at an ideal minimum ($\alpha \approx 1$). In this
33
34 case, the α value for device with SnO₂ and graphene-SnO₂ are increased from 0.971 to 0.986
35
36 by fitting the J_{sc} data, indicating the bimolecular recombination is suppressed upon the
37
38 incorporation of graphene in the SnO₂ ETL. In addition, in the open-circuit condition, the
39
40 performance of a PSC is determined by trap dominated monomolecular recombination when
41
42 ε approaches to 2. By comparison the ε value fitted from the V_{oc} data, it is obvious that the
43
44 monomolecular recombination in the device with graphene is greatly eliminated as the ε
45
46 value dropped from 1.74 to 1.59. Therefore, we believe the incorporation of graphene into
47
48 the SnO₂ ETL is not only beneficial for the enhancement of electron mobility and charge
49
50
51
52
53
54
55
56
57
58
59
60

1
2
3 extraction but also for suppressing the interface charge recombination by reducing the
4
5 interfacial defects.
6
7

8 The stability of our device was checked by steady-state measurements of PCE values. The
9
10 performance deviation at different times via the aging process measured under one sun
11
12 illumination with AM1.5 G is shown in Figure 6. After 300 hours, the PCE of the
13
14 un-encapsulated device without graphene dramatically decreased from 17.01% to 11.07%.
15
16 With the graphene-SnO₂ as ETL, the PCE of the device retained more than 90% of its initial
17
18 PCE, slightly dropped from 18.11% to 16.50% after 300 hours aging in the ambient condition
19
20 with a relative humidity of 40 ± 5%. Further contact angle measurements were carried out
21
22 on FTO substrates with SnO₂ layers and various content graphene-doped SnO₂ layers. It can
23
24 be seen that the contact angle increased from 52° to 74° while the volume of graphene
25
26 changed from 0% to 4% (v/v) (Figure S8) due to the hydrophobicity nature of graphene.⁵⁵
27
28 Embedded graphene also slowed down the perovskite degradation by trapped charges in
29
30 control devices. Therefore, the reduced amount of trapped charge at the interface of
31
32 graphene-SnO₂ and perovskite with respect to the reference device can certify the higher
33
34 stability afforded by the graphene-containing interface. Recently, Ahn and co-workers⁵⁶
35
36 demonstrated that higher density of trapped charge at the interface of mesoscopic TiO₂ and
37
38 perovskite results in more efficient activation of perovskite decomposition. The presence of
39
40 both stored charge and access to moisture are necessary for rapid decomposition of the
41
42 perovskite. The reasons are still unknown, but according to this work we believe that the 2D
43
44 layer structured graphene with good chemical stability and ion implantation capability into
45
46 the active layer structure for steadiness is beneficial to the long-term stability.
47
48
49
50
51
52
53
54
55
56
57
58
59
60

3. Conclusion

1
2
3 In conclusion, we have reported a low-temperature and solution processed graphene ink
4
5 doping SnO₂ nanoparticles as the electron transport layer for planar structured PSCs, and
6
7
8 over 18% power conversion efficiency with negligible hysteresis was obtained. The
9
10 graphene-SnO₂ PSC exhibits a respectable ambient stability without encapsulation, with
11
12 retention of 90% of the initial PCE after aging in ambient condition with a relative humidity
13
14 of 40 ± 5% for 300 hours. Incorporation of the graphene in the SnO₂ matrix has been proven
15
16 to be an effective strategy to simultaneously enhance the electron mobility, carrier
17
18 extraction ability and suppress the interfacial charge recombination. This study provides
19
20 important insight for further research in utilizing graphene materials for planar PSCs from
21
22 low-temperature solution process.
23
24
25
26
27
28
29

30 **4. Experimental Section**

31 *Materials*

32
33 All reagents were purchased from Sigma-Aldrich and used as received, including PbI₂
34
35 (99.999%), isopropanol (99.99%), N, N-dimethylformamide (99.99%), 4-tert-butylpyridine
36
37 (99.9%), chlorobenzene (99.9%), acetonitrile (99.9%). Spiro-OMeTAD (Canada 1materials),
38
39 fluorine-doped tin oxide (FTO, Japan Asahi Glass) with a sheet resistance of 14 Ω sq⁻¹ on glass
40
41 was purchased. The purity of the gold used for the top contact electrode is 99.99%.
42
43
44
45
46

47 *Graphene ink synthesis*

48
49 A composite of graphene and ethyl cellulose was prepared following previously reported
50
51 methods.⁵⁶ Graphene was prepared by mechanical exfoliation by high-shear mixer. A mixture
52
53 containing flake graphite (Qingdao Grade Pure, 20% w/v), ethyl cellulose (Sigma Aldrich, 4 cP
54
55 grade, 1.5% w/v), and ethanol was processed with a high-shear mixer operating at 10,000
56
57 rpm for 3 h. Centrifugation (8000 rpm for 10 minutes, followed by 5000 rpm for 120
58
59
60

1
2
3 minutes) was performed to remove the large unexfoliated graphite particles. Salt water
4
5 (0.04 mg/mL) was added to the as-obtained dispersion containing graphene, ethyl cellulose,
6
7 and ethanol as flocculate in a 16:9 wt. ratio and centrifuged at 8000 rpm for 8 minutes and
8
9 collect the graphene/ethyl cellulose composite. This composite was then dispersed in water,
10
11 vacuum filtered through 0.45 μm filter paper, and dried to yield a fine black powder which
12
13 contained 34% wt. graphene and 66% wt. ethyl cellulose.
14
15
16

17 *SnO₂ ETL preparation*

18
19 FTO substrate was ultrasonically cleaned with detergent solution, acetone, deionized water
20
21 and isopropanol in sequence. The substrated was first UV-ozone treated for 15 minutes. The
22
23 SnO₂ film was spin coated with 0.1 M SnCl₂·2H₂O ethanol solution and annealed at 100 °C for
24
25 60 minutes, 180 °C for 60 minutes in air with a thickness around 50 nm.
26
27
28

29
30 For graphene/SnO₂ ETLs, a precursor solution of graphene/ethyl cellulose (EC) and SnCl₂ in
31
32 ethanol was stirred at room temperature for 10 minutes, then spin coated onto FTO
33
34 substrates at 2500 rpm for 30 seconds. Then the graphene/EC-SnO₂ thin films were heated
35
36 in at 100 °C for 60 minutes and 180 °C for 60 minutes in air.^{58, 59}
37
38
39

40 *Solar cell fabrication*

41
42 SnO₂ and graphene-SnO₂ ETLs need 15 minutes of UV-O₃ treatments before used, 461 mg of
43
44 PbI₂, 159 mg of CH₃NH₃I were dissolved in 800 μL dimethylformamide (DMF) and dimethyl
45
46 sulfoxide (DMSO) with a volume ratio (4:1) was stirred at room temperature for 1hour. Then,
47
48 the perovskite precursor solution was spin coated onto the FTO/SnO₂ substrate with a speed
49
50 2500 rpm for 60 seconds and 550 μL of diethylether was dipped onto rotating substrate in
51
52 3seconds before the surface changed to be turbid. The as-prepared perovskite film was
53
54 annealed at 100 °C for 10 mininutes to obtain a perovskite film. A 30 μL of spiro-OMeTAD
55
56 solution was spin coated on the surface of perovskite film at 3000 rpm for 30 seconds.⁵⁸
57
58
59
60

1
2
3 Lastly, an 80 nm gold layer was deposited through shadow masks via thermal evaporation
4
5 under high vacuum. The active areas were 0.09 cm² and 0.39 cm².
6
7

8 *Characterization*

9

10 Scanning electron microscopic (SEM) tests were performed with a Zeiss Supra 40 FE SEM
11
12 with an accelerating voltage of 10 kV. Transmission electron microscopy (TEM) was
13
14 performed on an electron microscope (H-7650, Japan) with an acceleration voltage of 80 kV.
15
16 Ultraviolet-visible absorption spectra were recorded on a Shimadzu UV-3101
17
18 spectrophotometer at room temperature. PL spectra were collected using a confocal system
19
20 with 100X, using excitation of wavelength 395 nm. Raman spectra was collected using a
21
22 confocal Raman system with 532 nm excitation. The surface morphologies were
23
24 characterized by atomic force microscopy (AFM, SPM-9500j3). *J-V* tests were carried out
25
26 with an electrochemical workstation (BAS100B electrochemical analyzer, Bioanalytical
27
28 Systems Inc., USA) under AM1.5 G (1 sun conditions, 100 mW cm⁻²). External quantum
29
30 efficiency (EQE) was measured by a Xenon lamp (Newport) attached to a monochromator
31
32 (Newport). Two lenses were used to focus a monochromatic light on an active area of a PSC.
33
34 Time-resolved photoluminescence spectroscopy (TRPL) was performed using a streak
35
36 camera setup (Hamamatsu C4334 Streakscope) similar to our previous work.⁵⁸ X-ray
37
38 photoelectron spectroscopy (XPS, ESCALAB 250Xi) was used to measure the composition of
39
40 the as-fabricated electrodes.
41
42
43
44
45
46
47
48
49
50
51
52

53 **Supporting Information:**

54
55 AFM of the graphene flakes, TEM and Raman of graphene/SnO₂, SEM of bare FTO and
56
57 graphene/SnO₂ electrode, *J-V* curves and histogram of the PCE of devices with
58
59 graphene/SnO₂, contact angle measurement of graphene/SnO₂ electrodes.
60

Acknowledgements

This work was financially supported by the National Natural Science Foundation of China NSFC (51702038) and the Recruitment Program for Young Professionals. At Northwestern this work was supported in part by the ANSER Center, an Energy Frontier Research Center funded by the U.S. Department of Energy, Office of Science, and Office of Basic Energy Sciences under Award DE-SC0001059.

References

1. Kojima, A.; Teshima, K.; Shirai, Y.; Miyasaka, T., Organometal Halide Perovskites as Visible-Light Sensitizers for Photovoltaic Cells. *J. Am. Chem. Soc.* 2009, 131, 6050-6051.
2. Lee, M. M.; Teuscher, J.; Miyasaka, T.; Murakami, T. N.; Snaith, H. J., Efficient Hybrid Solar Cells Based on Meso-Superstructured Organometal Halide Perovskites. *Science* 2012, 338, 1228604.
3. Zhou, H.; Chen, Q.; Li, G.; Luo, S.; Song, T.-b.; Duan, H.-S.; Hong, Z.; You, J.; Liu, Y.; Yang, Y., Interface Engineering of Highly Efficient Perovskite Solar Cells. *Science* 2014, 345, 542-546.
4. Green, M. A.; Hishikawa, Y.; Dunlop, E. D.; Levi, D. H.; Hohl-Ebinger, J.; Ho-Baillie, A. W. Y., Solar Cell Efficiency Tables (Version 52). *Prog. Photovoltaics* 2018, 26, 427-436.
5. Yang, W. S.; Noh, J. H.; Jeon, N. J.; Kim, Y. C.; Ryu, S.; Seo, J.; Seok, S. I., High-Performance Photovoltaic Perovskite Layers Fabricated through Intramolecular Exchange. *Science* 2015, 348, 1234-1237.

- 1
2
3 6. Research Cell Efficiency Records, Nrel, <http://www.nrel.gov/ncpv/>, Accessed: July, 2018.
- 4
5
6 7. Kagan, C. R.; Mitzi, D. B.; Dimitrakopoulos, C. D., Organic-Inorganic Hybrid Materials as
7
8 Semiconducting Channels in Thin-Film Field-Effect Transistors. *Science* 1999, 286, 945-947.
- 9
10
11 8. Xing, G.; Mathews, N.; Sun, S.; Lim, S. S.; Lam, Y. M.; Gratzel, M.; Mhaisalkar, S.; Sum, T.
12
13 C., Long-Range Balanced Electron- and Hole-Transport Lengths in Organic-Inorganic
14
15 $\text{CH}_3\text{NH}_3\text{PbI}_3$. *Science* 2013, 342, 344-347.
- 16
17
18 9. Stranks, S. D.; Eperon, G. E.; Grancini, G.; Menelaou, C.; Alcocer, M. J. P.; Leijtens, T.;
19
20 Herz, L. M.; Petrozza, A.; Snaith, H. J., Electron-Hole Diffusion Lengths Exceeding 1
21
22 Micrometer in an Organometal Trihalide Perovskite Absorber. *Science* 2013, 342, 341-344.
- 23
24
25 10. Gratzel, M., The Light and Shade of Perovskite Solar Cells. *Nat. Mater.* 2014, 13,
26
27 838-842.
- 28
29
30 11. Liu, M. Z.; Johnston, M. B.; Snaith, H. J., Efficient Planar Heterojunction Perovskite Solar
31
32 Cells by Vapour Deposition. *Nature* 2013, 501, 395-398.
- 33
34
35 12. Burschka, J.; Pellet, N.; Moon, S. J.; Humphry-Baker, R.; Gao, P.; Nazeeruddin, M. K.;
36
37 Gratzel, M., Sequential Deposition as a Route to High-Performance Perovskite-Sensitized
38
39 Solar Cells. *Nature* 2013, 499, 316-319.
- 40
41
42 13. van Reenen, S.; Kemerink, M.; Snaith, H. J., Modeling Anomalous Hysteresis in
43
44 Perovskite Solar Cells. *J. Phys. Chem. Lett.* 2015, 6, 3808-3814.
- 45
46
47 14. Zhang, Y.; Liu, M. Z.; Eperon, G. E.; Leijtens, T. C.; McMeekin, D.; Saliba, M.; Zhang, W.;
48
49 de Bastiani, M.; Petrozza, A.; Herz, L. M.; Johnston, M. B.; Lin, H.; Snaith, H. J., Charge
50
51 Selective Contacts, Mobile Ions and Anomalous Hysteresis in Organic-Inorganic Perovskite
52
53 Solar Cells. *Mater. Horiz.* 2015, 2, 315-322.
- 54
55
56 15. Tress, W.; Marinova, N.; Moehl, T.; Zakeeruddin, S. M.; Nazeeruddin, M. K.; Gratzel, M.,
57
58 Understanding the Rate-Dependent J-V Hysteresis, Slow Time Component, and Aging in
59
60

- 1
2
3 CH₃NH₃PbI₃ Perovskite Solar Cells: The Role of a Compensated Electric Field. *Energy Environ.*
4
5 *Sci.* 2015, 8, 995-1004.
6
7
8 16. Seo, J. Y.; Matsui, T.; Luo, J. S.; Correa-Baena, J. P.; Giordano, F.; Saliba, M.; Schenk, K.;
9
10 Ummadisingu, A.; Domanski, K.; Hadadian, M.; Hagfeldt, A.; Zakeeruddin, S. M.; Steiner, U.;
11
12 Gratzel, M.; Abate, A., Ionic Liquid Control Crystal Growth to Enhance Planar Perovskite Solar
13
14 Cells Efficiency. *Adv. Energy. Mater.*, 2016, 6, 1600767.
15
16
17 17. Zhang, Y.; Fei, Z. F.; Gao, P.; Lee, Y. H.; Tirani, F. F.; Scopelliti, R.; Feng, Y. Q.; Dyson, P. J.;
18
19 Nazeeruddin, M. K., A Strategy to Produce High Efficiency, High Stability Perovskite Solar
20
21 Cells Using Functionalized Ionic Liquid-Dopants. *Adv. Mater.*, 2017, 29, 1702157.
22
23
24 18. Sandoval-Torrientes, R.; Pascual, J.; Garcia-Benito, I.; Collavini, S.; Kosta, I.; Tena-Zaera,
25
26 R.; Martin, N.; Delgado, J. L., Modified Fullerenes for Efficient Electron Transport Layer-Free
27
28 Perovskite/Fullerene Blend-Based Solar Cells. *ChemSusChem* 2017, 10, 2023-2029.
29
30
31 19. Zhao, D. W.; Ke, W. J.; Grice, C. R.; Cimaroli, A. J.; Tan, X. X.; Yang, M. J.; Collins, R. W.;
32
33 Zhang, H. M.; Zhu, K.; Yan, Y. F., Annealing-Free Efficient Vacuum-Deposited Planar
34
35 Perovskite Solar Cells with Evaporated Fullerenes as Electron-Selective Layers. *Nano Energy*
36
37 2016, 19, 88-97.
38
39
40 20. Park, M.; Kim, J. Y.; Son, H. J.; Lee, C. H.; Jang, S. S.; Ko, M. J., Low-Temperature
41
42 Solution-Processed Li-Doped SnO₂ as an Effective Electron Transporting Layer for
43
44 High-Performance Flexible and Wearable Perovskite Solar Cells. *Nano Energy* 2016, 26,
45
46 208-215.
47
48
49 21. Jiang, Q.; Zhang, L. Q.; Wang, H. L.; Yang, X. L.; Meng, J. H.; Liu, H.; Yin, Z. G.; Wu, J. L.;
50
51 Zhang, X. W.; You, J. B., Enhanced Electron Extraction Using SnO₂ for High-Efficiency
52
53 Planar-Structure HC(NH₂)₂PbI₃-Based Perovskite Solar Cells. *Nat. Energy* 2017, 2, 1-7.
54
55
56
57
58
59
60

- 1
2
3 22. Yang, G.; Lei, H. W.; Tao, H.; Zheng, X. L.; Ma, J. J.; Liu, Q.; Ke, W. J.; Chen, Z. L.; Xiong, L.
4
5 B.; Qin, P. L.; Chen, Z.; Qin, M. C.; Lu, X. H.; Yan, Y. F.; Fang, G. J., Reducing Hysteresis and
6
7 Enhancing Performance of Perovskite Solar Cells Using Low-Temperature Processed Y-Doped
8
9 SnO₂ Nanosheets as Electron Selective Layers. *Small* 2017, 13, 1601769.
10
11
12 23. Tiwana, P.; Docampo, P.; Johnston, M. B.; Snaith, H. J.; Herz, L. M., Electron Mobility and
13
14 Injection Dynamics in Mesoporous ZnO, SnO₂, and TiO₂ Films Used in Dye-Sensitized Solar
15
16 Cells. *ACS Nano* 2011, 5, 5158-5166.
17
18
19 24. Zhang, J.; Chen, R. J.; Wu, Y. Z.; Shang, M. H.; Zeng, Z. B.; Zhang, Y.; Zhu, Y. J.; Han, L. Y.,
20
21 Extrinsic Movable Ions in MAPbI₃ Modulate Energy Band Alignment in Perovskite Solar Cells.
22
23 *Adv. Energy Mater*, 2018, 8, 1701981.
24
25
26 25. Baena, J. P. C.; Steier, L.; Tress, W.; Saliba, M.; Neutzner, S.; Matsui, T.; Giordano, F.;
27
28 Jacobsson, T. J.; Kandada, A. R. S.; Zakeeruddin, S. M.; Petrozza, A.; Abate, A.; Nazeeruddin,
29
30 M. K.; Gratzel, M.; Hagfeldt, A., Highly Efficient Planar Perovskite Solar Cells through Band
31
32 Alignment Engineering. *Energ Environ. Sci.*, 2015, 8, 2928-2934.
33
34
35 26. Liu, X.; Tsai, K. W.; Zhu, Z.; Sun, Y.; Chueh, C. C.; Jen, A. K. Y., A Low-Temperature,
36
37 Solution Processable Tin Oxide Electron-Transporting Layer Prepared by the Dual-Fuel
38
39 Combustion Method for Efficient Perovskite Solar Cells. *Adv. Mater. Interfaces* 2016, 3,
40
41 1600122.
42
43
44 27. Ma, J. J.; Yang, G.; Qin, M. C.; Zheng, X. L.; Lei, H. W.; Chen, C.; Chen, Z. L.; Guo, Y. X.; Han,
45
46 H. W.; Zhao, X. Z.; Fang, G. J., MgO Nanoparticle Modified Anode for Highly Efficient
47
48 SnO₂-Based Planar Perovskite Solar Cells. *Adv. Sci.*, 2017, 4, 1700031.
49
50
51 28. Lee, Y.; Lee, S.; Seo, G.; Paek, S.; Cho, K. T.; Huckaba, A. J.; Calizzi, M.; Choi, D. W.; Park, J.
52
53 S.; Lee, D.; Lee, H. J.; Asiri, A. M.; Nazeeruddin, M. K., Efficient Planar Perovskite Solar Cells
54
55 Using Passivated Tin Oxide as an Electron Transport Layer. *Adv. Sci.*, 2018, 5, 1800130.
56
57
58
59
60

- 1
2
3 29. Chen, B.; Yang, M. J.; Priya, S.; Zhu, K., Origin of J-V Hysteresis in Perovskite Solar Cells. *J.*
4
5
6 *Phys. Chem. Lett.*, 2016, 7, 905-917.
7
8 30. Chen, H. W.; Sakai, N.; Ikegami, M.; Miyasaka, T., Emergence of Hysteresis and Transient
9
10
11
12
13
14 31. Hou, Y.; Scheiner, S.; Tang, X. F.; Gasparini, N.; Richter, M.; Li, N.; Schweizer, P.; Chen, S.;
15
16
17
18
19
20
21
22
23
24 32. Kim, H. S.; Jang, I. H.; Ahn, N.; Choi, M.; Guerrero, A.; Bisquert, J.; Park, N. G., Control of
25
26
27
28
29
30
31
32
33
34
35
36
37
38
39
40
41
42
43
44
45
46
47
48
49
50
51
52
53
54
55
56
57
58
59
60
- Chen, H. W.; Quiroz, C. O. R.; Du, X. Y.; Matt, G. J.; Osvet, A.; Spiecker, E.; Fink, R. H.; Hirsch, A.; Halik, M.; Brabec, C. J., Suppression of Hysteresis Effects in Organohalide Perovskite Solar Cells. *Adv. Mater. Interfaces* 2017, 4, 1245011.
- I-V Hysteresis in CH₃NH₃PbI₃ Perovskite Solar Cell. *J. Phys. Chem. Lett.*, 2015, 6, 4633-4639.
33. Kim, H. S.; Park, N. G., Parameters Affecting I-V Hysteresis of CH₃NH₃PbI₃ Perovskite Solar Cells: Effects of Perovskite Crystal Size and Mesoporous TiO₂ Layer *J. Phys. Chem. Lett.* 2014, 5, 3434-3434.
34. Ke W., Zhao D., Xiao C., Wang C., Cimaroli A.J., Grice C.R., Yang M., Li Z. Jiang C., Mowafak A.J., Zhu K., Kanatzidis M.G., Fang G. and Yan Y., Cooperative Tin oxide Fullerene Electron Selective Layers for High-performance Planar Perovskite Solar Cells. *J Mater. Chem. A.* 2016,4, 14276-14283.
35. Hou, Y.; Quiroz, C. O. R.; Scheiner, S.; Chen, W.; Stubhan, T.; Hirsch, A.; Halik, M.; Brabec, C. J., Low-Temperature and Hysteresis-Free Electron-Transporting Layers for Efficient, Regular, and Planar Structure Perovskite Solar Cells. *Adv. Energy. Mater.*, 2015, 5, 1501056.
36. Mahmood, K.; Swain, B. S.; Amassian, A., 16.1% Efficient Hysteresis-Free Mesostructured Perovskite Solar Cells Based on Synergistically Improved ZnO Nanorod Arrays. *Adv. Energy. Mater.*, 2015, 5, 1500568.

- 1
2
3 37. Wang, C. L.; Xiao, C. X.; Yu, Y.; Zhao, D. W.; Awni, R. A.; Grice, C. R.; Ghimire, K.;
4
5 Constantinou, I.; Liao, W. Q.; Cimaroli, A. J.; Liu, P.; Chen, J.; Podraza, N. J.; Jiang, C. S.;
6
7 Al-Jassim, M. M.; Zhao, X. Z.; Yan, Y. F., Understanding and Eliminating Hysteresis for Highly
8
9 Efficient Planar Perovskite Solar Cells. *Adv. Energy. Mater.*, 2017, 7, 1700414.
10
11
12 38. Wang, Y. C.; Li, X. D.; Zhu, L. P.; Liu, X. H.; Zhang, W. J.; Fang, J. F., Efficient and
13
14 Hysteresis-Free Perovskite Solar Cells Based on a Solution Processable Polar Fullerene
15
16 Electron Transport Layer. *Adv. Energy. Mater.*, 2017, 7, 1701144.
17
18
19 39. Cao, J.; Wu, B. H.; Chen, R. H.; Wu, Y. Y. Q.; Hui, Y.; Mao, B. W.; Zheng, N. F., Efficient,
20
21 Hysteresis-Free, and Stable Perovskite Solar Cells with ZnO as Electron-Transport Layer:
22
23 Effect of Surface Passivation. *Adv. Mater.*, 2018, 30, 1705596.
24
25
26 40. Ke, W.; Fang, G.; Liu, Q.; Xiong, L.; Qin, P.; Tao, H.; Wang, J.; Lei, H.; Li, B.; Wan, J.,
27
28 Low-Temperature Solution-Processed Tin Oxide as an Alternative Electron Transporting
29
30 Layer for Efficient Perovskite Solar Cells. *J. Am. Chem. Soc.*, 2015, 137, 6730-6733.
31
32
33 41. Zuo, L.; Guo, H.; Jariwala, S.; De Marco, N.; Dong, S.; DeBlock, R.; Ginger, D. S.; Dunn, B.;
34
35 Wang, M.; Yang, Y., Polymer-Modified Halide Perovskite Films for Efficient and Stable Planar
36
37 Heterojunction Solar Cells. *Sci. Adv.*, 2017, 3, e1700106.
38
39
40 42. Kim, H.-S.; Park, N.-G., Parameters Affecting I–V Hysteresis of CH₃NH₃PbI₃ Perovskite
41
42 Solar Cells: Effects of Perovskite Crystal Size and Mesoporous TiO₂ Layer. *J. Phys. Chem. Lett.*
43
44 2014, 5, 2927-2934.
45
46
47 43. Tress, W.; Marinova, N.; Moehl, T.; Zakeeruddin, S. M.; Nazeeruddin, M. K.; Grätzel, M.,
48
49 Understanding the Rate-Dependent J–V Hysteresis, Slow Time Component, and Aging in
50
51 CH₃NH₃PbI₃ Perovskite Solar Cells: The Role of a Compensated Electric Field. *Energy Environ.*
52
53 *Sci.*, 2015, 8, 995-1004.
54
55
56
57
58
59
60

- 1
2
3 44. Azpiroz, J. M.; Mosconi, E.; Bisquert, J.; De Angelis, F., Defect Migration in
4
5 Methylammonium Lead Iodide and Its Role in Perovskite Solar Cell Operation. *Energy*
6
7
8 *Environ. Sci.* 2015, 8, 2118-2127.
9
- 10 45. Chen, B.; Yang, M.; Priya, S.; Zhu, K., Origin of J–V Hysteresis in Perovskite Solar Cells. *J.*
11
12 *Phys. Chem. Lett.* 2016, 7, 905-917.
13
- 14 46. Li, C.; Tscheuschner, S.; Paulus, F.; Hopkinson, P. E.; Kießling, J.; Köhler, A.; Vaynzof, Y.;
15
16 Huettner, S., Iodine Migration and Its Effect on Hysteresis in Perovskite Solar Cells. *Adv*
17
18 *Mater* 2016, 28, 2446-2454.
19
- 20 47. Zhu, M.; Li, X.; Liu, W.; Cui, Y., An Investigation on the Photoelectrochemical Properties
21
22 of Dye-Sensitized Solar Cells Based on Graphene–TiO₂ Composite Photoanodes. *J. Power*
23
24 *Sources* 2014, 262, 349-355.
25
- 26 48. Jiang, H.; Yan, Z.; Zhao, H.; Yuan, S.; Yang, Z.; Li, J.; Liu, B.; Niu, T.; Feng, J.; Wang, Q.,
27
28 Bifunctional Hydroxylamine Hydrochloride Incorporated Perovskite Films for Efficient and
29
30 Stable Planar Perovskite Solar Cells. *ACS Appl. Energy Mater.* 2018, 1, 900-909.
31
32
- 33 49. Xie, J.; Huang, K.; Yu, X.; Yang, Z.; Xiao, K.; Qiang, Y.; Zhu, X.; Xu, L.; Wang, P.; Cui, C.,
34
35 Enhanced Electronic Properties of SnO₂ Via Electron Transfer from Graphene Quantum Dots
36
37 for Efficient Perovskite Solar Cells. *ACS Nano* 2017, 11, 9176-9182.
38
39
- 40 50. Agresti, A.; Pescetelli, S.; Taheri, B.; Del Rio Castillo, A. E.; Cinà, L.; Bonaccorso, F.; Di
41
42 Carlo, A., Graphene–Perovskite Solar Cells Exceed 18% Efficiency: A Stability Study.
43
44 *ChemSusChem* 2016, 9, 2609-2619.
45
46
- 47 51. Li, H.; Tao, L.; Huang, F.; Sun, Q.; Zhao, X.; Han, J.; Shen, Y.; Wang, M., Enhancing
48
49 Efficiency of Perovskite Solar Cells via Surface Passivation with Graphene Oxide Interlayer.
50
51 *ACS Appl. Mater. Inter.* 2017, 9, 38967-38976.
52
53
54
55
56
57
58
59
60

- 1
2
3 52. Agresti, A.; Pescetelli, S.; Palma, A. L.; Del Rio Castillo, A. E.; Konios, D.; Kakavelakis, G.;
4
5 Razza, S.; Cinà, L.; Kymakis, E.; Bonaccorso, F., Graphene Interface Engineering for Perovskite
6
7 Solar Modules: 12.6% Power Conversion Efficiency over 50 cm² Active Area. *ACS Energy Lett.*
8
9 2017, 2, 279-287.
10
11
12 53. Lu, K.; Wang, Y.; Yuan, J.; Cui, Z.; Shi, G.; Shi, S.; Han, L.; Chen, S.; Zhang, Y.; Ling, X.,
13
14 Efficient PbS Quantum Dot Solar Cells Employing a Conventional Structure. *J Mater. Chem. A*
15
16 2017, 5, 23960-23966.
17
18
19 54. Cai, F.; Cai, J.; Yang, L.; Li, W.; Gurney, R. S.; Yi, H.; Iraqi, A.; Liu, D.; Wang, T., Molecular
20
21 Engineering of Conjugated Polymers for Efficient Hole Transport and Defect Passivation in
22
23 Perovskite Solar Cells. *Nano Energy* 2018, 45, 28-36.
24
25
26 55. Zhao, X.; Tao, L.; Li, H.; Huang, W.; Sun, P.; Liu, J.; Liu, S.; Sun, Q.; Cui, Z.; Sun, L., Efficient
27
28 Planar Perovskite Solar Cells with Improved Fill Factor via Interface Engineering with
29
30 Graphene. *Nano Lett.* 2018, 18, 2442-2449.
31
32
33 56. Ahn, N.; Son, D.-Y.; Jang, I.-H.; Kang, S. M.; Choi, M.; Park, N.-G., Highly Reproducible
34
35 Perovskite Solar Cells with Average Efficiency of 18.3% and Best Efficiency of 19.7%
36
37 Fabricated via Lewis Base Adduct of Lead (II) Iodide. *J. Am. Chem. Soc.* 2015, 137, 8696-8699.
38
39
40 57. Secor, E. B.; Ahn, B. Y.; Gao, T. Z.; Lewis, J. A.; Hersam, M. C., Rapid and Versatile
41
42 Photonic Annealing of Graphene Inks for Flexible Printed Electronics. *Adv. Mater.*, 2015, 27,
43
44 6683-6688.
45
46
47 58. Zhu, M.; Liu, W.; Ke, W.; Clark, S.; Secor, E. B.; Song, T.-B.; Kanatzidis, M. G.; Li, X.;
48
49 Hersam, M. C., Millisecond-Pulsed Photonic-Annealed Tin Oxide Electron Transport
50
51 Layers for Efficient Perovskite Solar Cells. *J. Mater. Chem. A* 2017, 5, 24110-24115.
52
53
54
55
56
57
58
59
60

1
2
3 59. Burschka, J.; Pellet, N.; Moon, S.-J.; Humphry-Baker, R.; Gao, P.; Nazeeruddin, M. K.;
4
5 Grätzel, M., Sequential Deposition as a Route to High-Performance Perovskite-Sensitized
6
7
8 Solar Cells. *Nature* 2013, 499, 316-319.
9
10
11
12
13
14
15
16
17
18
19
20
21
22
23
24
25
26
27
28
29
30
31
32
33
34
35
36
37
38
39
40
41
42
43
44
45
46
47
48
49
50
51
52
53
54
55
56
57
58
59
60

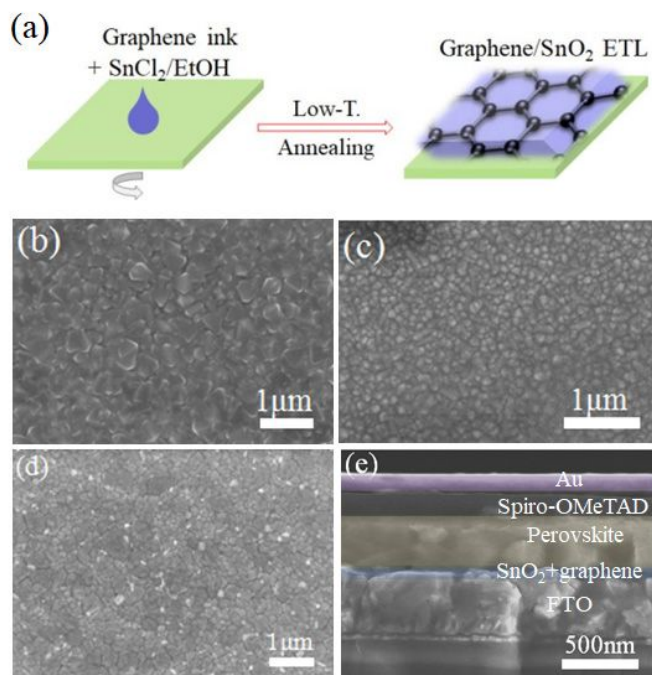


Figure 1 Fabrication of PSCs based on solution processed graphene doping SnO_2 . (a) Solvent engineering procedure with spin-coating scheme for preparing SnO_2 -graphene ET; (b) top-view SEM images of the layer by layer deposition process: SnO_2 ; (c) SnO_2 -graphene deposited by spin coating; (d) the perovskite crystals grown on top and (e) cross-sectional SEM of a typical planar PSC architecture FTO/ SnO_2 -graphene/perovskite/spiro-MeOTAD/Gold.

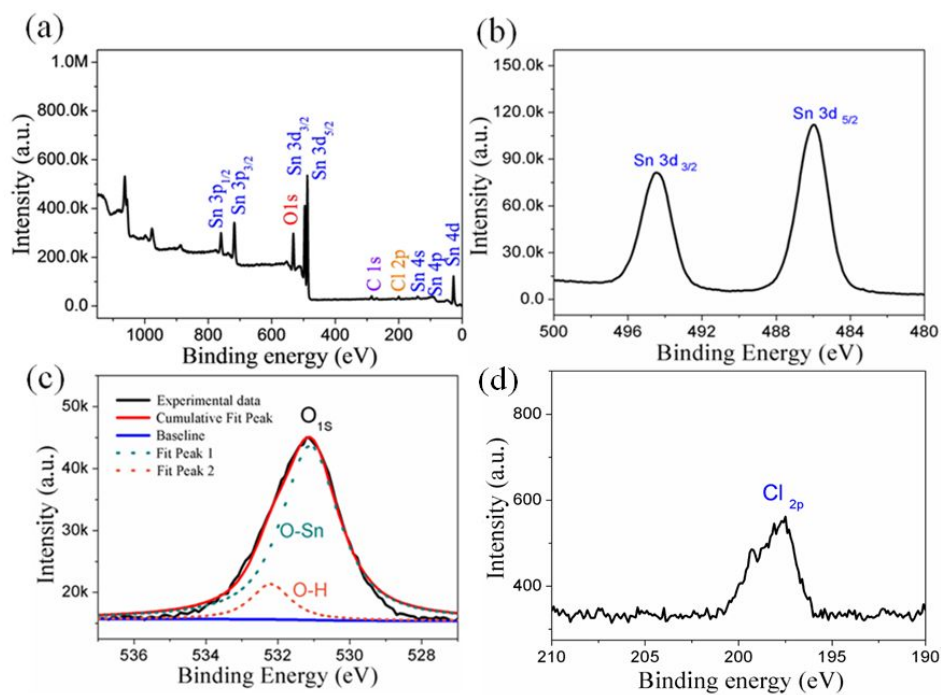


Figure 2 XPS spectra of a SnO₂-graphene film coated on an FTO substrate: (a) survey, (b) Sn 3d, (c) O 1s, and (d) Cl 2p.

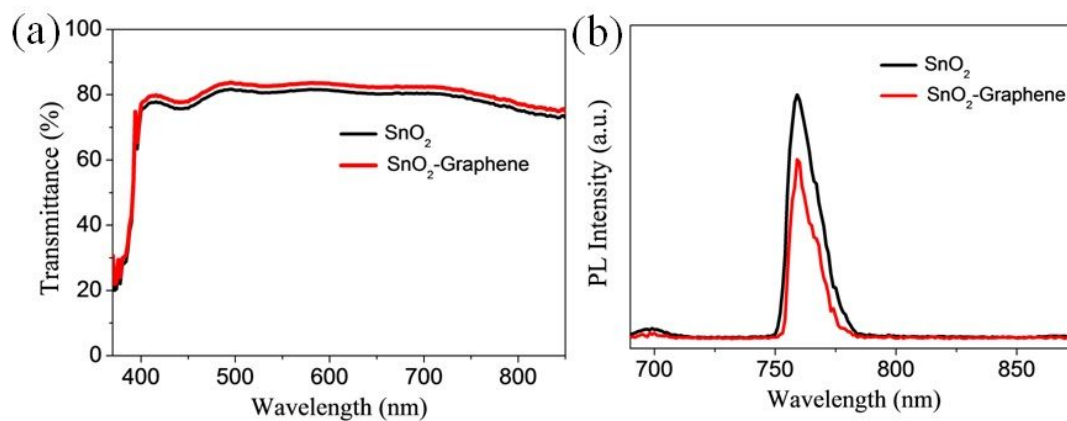


Figure 3 Optical property of SnO₂ and SnO₂-graphene: (a) transmission spectra and (b) photoluminescence spectrum.

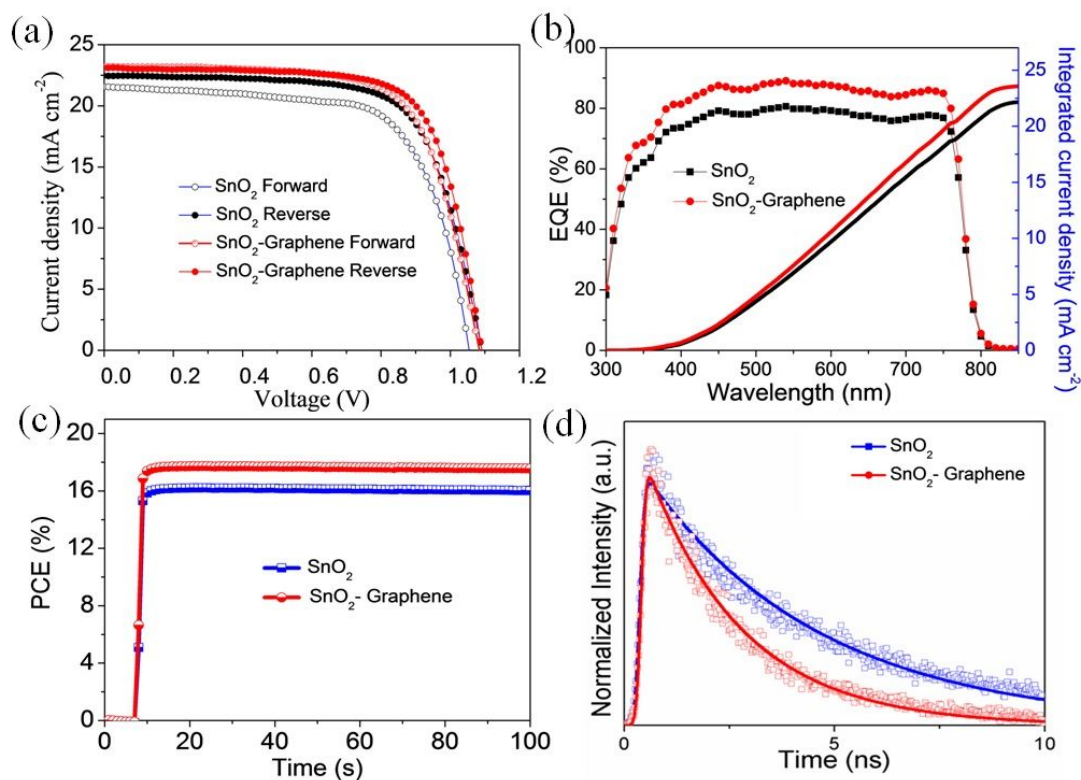


Figure 4 Photovoltaic performance. (a) J - V curves of the best-performing PSCs based on SnO₂ and SnO₂-graphene measured at reverse and forward scans; (b) EQE spectra of the best-performing cells based on SnO₂ and SnO₂-graphene; (c) Stabilized PCEs measured as a function of time for the SnO₂ and SnO₂-graphene based devices biased at their respective V_{mp} 0.925 V and 0.872 V, respectively and (d) Normalized time resolved photoluminescence response of the perovskite film fabricated on SnO₂ and graphene-SnO₂ ETLs.

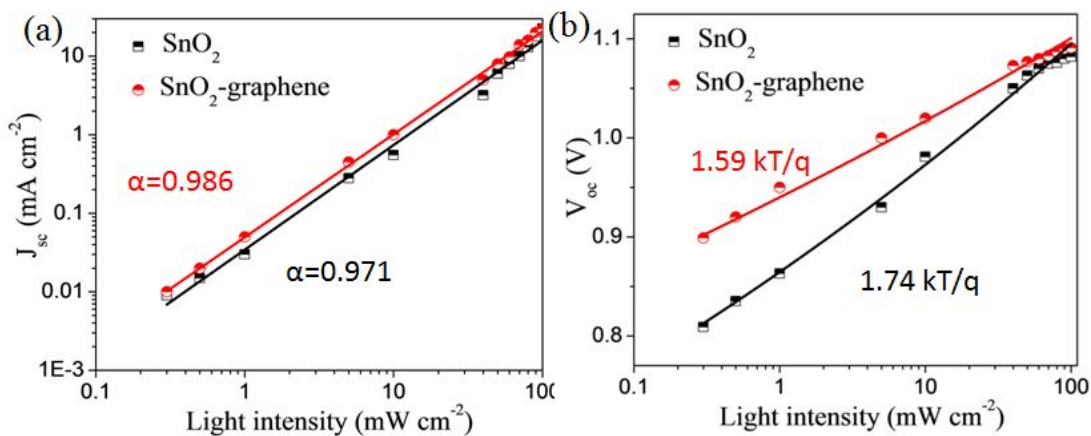


Figure 5 (a) J_{sc} and (b) V_{oc} dependence on light intensity for two devices with different ETLs.

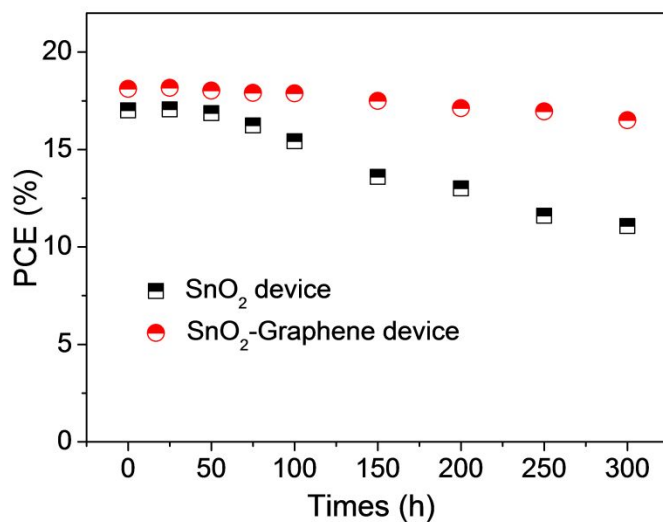


Figure 6 Stability of encapsulated devices SnO₂ and SnO₂-graphene placed at a ventilated cabinet over 300 hours with 40 ± 5% relative humidity at room temperature in the dark. The normalized PCE was tracked every 24 hours.

Table 1 Photovoltaic parameters of the PSCs with different ETLs under different scanning direction

ETLs	Scan directions	J_{sc} (mA cm ⁻²)	V_{oc} (V)	FF	PCE (%)	hysteresis index
SnO ₂	forward	21.55	1.054	0.68	15.45	0.08
	reverse	22.46	1.082	0.70	17.01	
SnO ₂ -Graphene	forward	23.21	1.084	0.69	17.36	0.02
	reverse	23.06	1.091	0.72	18.11	

TOC:

